Large-Signal Stability of Phase-Balanced Equilibria in Single-Phase Grid-Forming Inverter Systems

Minghui Lu, *Member, IEEE*, Weiqian Cai, *Student Member, IEEE*, Sairaj Dhople, *Senior Member, IEEE*, and Brian Johnson, *Senior Member, IEEE*

***Abstract*—This article explores the setup where large numbers of single-phase grid-forming inverters with droop control across distribution networks self-organize into a stable and balanced system with 120° phase offsets across aggregates in the absence of balanced three-phase generating resources or external communication. A suite of circuit- and system-theoretic notions are leveraged to derive a dynamical model for phase-angle differences across aggregates of inverters connected in the three phases. Focusing on this model, large-signal stability is established and the region of attraction of the phase-balanced equilibria is determined with the aid of a Lyapunov function. Experimental validation for a bench-top prototype network is included to support the analytical developments. Overall, the effort supports the vision of facilitating balanced operation of distribution networks with grid-forming inverters during service disruptions at the bulk transmission network.**

***Index Terms*—Droop control, grid-forming (GFM) inverters, Lyapunov stability, phase balancing, single-phase inverters.**

I. Introduction

GRID-FORMING (GFM) inverters are recognized to be enabling technologies for the integration of distributed renewable generation, storage systems, and electrified transportation across transmission and distribution networks [1]. Modeling, analysis, and control of GFM technologies across a diverse pool of applications is the subject of significant contemporary research [2]. We consider the particular setting of distribution networks with large numbers of single-phase droop-controlled GFM inverters interconnected to the subtransmission network through step-up delta-wye transformers (See Fig. 1). A variety of operational attributes are of interest in such a setting. We focus on the large-signal stability of phase-balanced equilibria, wherein aggregates of inverters across each of the phases settle to 120° phase offsets during islanded operation with no external communication between inverters across phases. Large-signal stability is established analytically with Lyapunov's direct method. Experimental validation for scaled prototypes is provided to support the analytical developments.

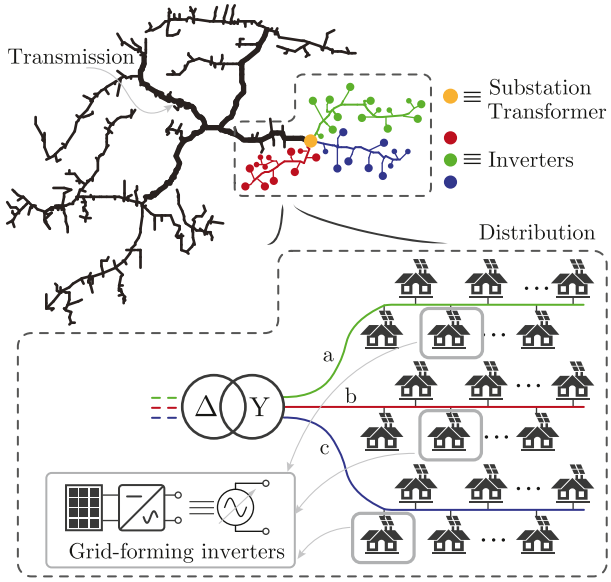

Fig. 1. Presence of massively distributed single-phase inverter-based generation gives the opportunity to realize ultraresilient systems capable of providing uninterruptible power. Our analysis shows that GFM droop controls facilitate communication-free phase balancing for single-phase inverters.

The effort extends our prior work [3], which demonstrated small-signal stability of phase-balanced equilibria for a collection of three single-phase delta-connected droop-controlled inverters serving a common load. While the setting in [3] is elementary, it provided a proof-of-concept into the intriguing possibility of achieving phase-balanced operation with GFM technologies. However, in real-world settings, we will indeed encounter scores of inverters in distribution networks; furthermore, small-signal stability, while critical, does not yield guarantees for ultraresilient operation in the face of a wide range of disturbances. Building on the work in [3], we consider the following setup which is admittedly more practical for the envisioned application: 1) multiple inverters with different ratings

Manuscript received 9 March 2023; revised 28 June 2023 and 20 August 2023; accepted 6 October 2023. Date of publication 24 October 2023; date of current version 26 January 2024. This work was supported in part by the U.S. Department of Energy under Grant EE0009025 and in part by the Office of Energy Efficiency and Renewable Energy (EERE) through Solar Energy Technologies Office (SETO) under Grant 38637 (UNIFI consortium). Recommended for publication by Associate Editor K. Basu. *(Minghui Lu and Weiqian Cai contributed equally to this work.) (Corresponding author: Brian Johnson.)*

Minghui Lu is with the Pacific Northwest National Laboratory, Richland, WA 99354 USA (e-mail: minghui.lu@pnnl.gov).

Weiqian Cai and Brian Johnson are with the Department of Electrical and Computer Engineering, University of Texas at Austin, Austin, TX 78712 USA (e-mail: stratoscwq@utexas.edu; b.johnson@utexas.edu).

Sairaj Dhople is with the Department of Electrical and Computer Engineering, University of Minnesota-Twin Cities, Minneapolis, MN 55455 USA (e-mail: sdhople@umn.edu).

Color versions of one or more figures in this article are available at https://doi.org/10.1109/TPEL.2023.3327234.

Digital Object Identifier 10.1109/TPEL.2023.3327234

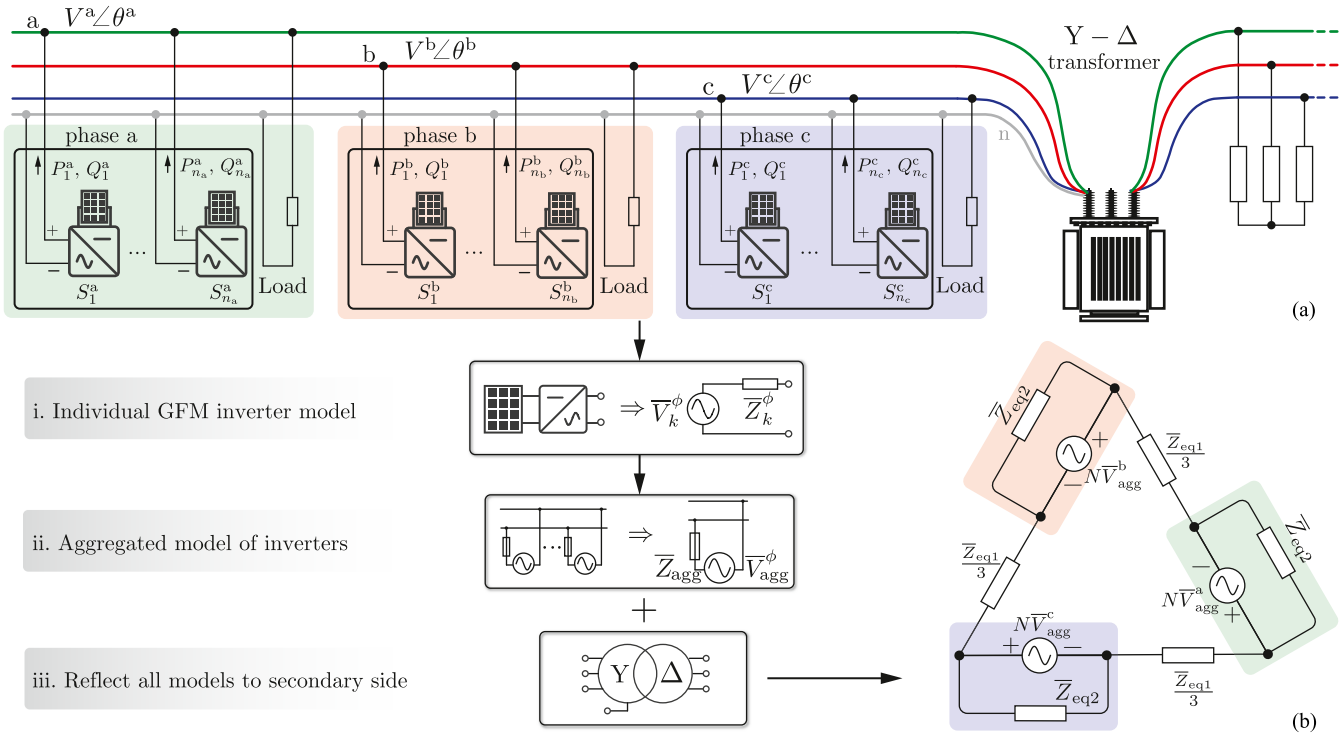

Fig. 2. (a) Overview of the system architecture and (b) the steps involved in obtaining a simplified equivalent-circuit network model. Section II presents details of the constituent elements of the system in (a) and Section III presents the steps involved in the derivation of the equivalent-circuit network model in (b).

are connected to each phase in a distribution network; 2) step-up delta-wye transformers are leveraged to interface the low-voltage distribution to a **high(er)-voltage (sub)transmission network. See Fig. 2 for a sketch of the system architecture. While the work in[3] considered small-signal stability, in this effort we prove large-signal stability and characterize the region of attraction (ROA) of phase-balanced equilibria for this more complex and realistic setting. We do so with the Lyapunov stability theory; and, the derivation of the dynamical model leveraged for stability assessment is based on the application of a wide number of circuit-theoretic constructs including aggregation, mesh analysis, and power-flow analysis. While we present results on large-signal stability, we refrain from dwelling on current-limiting operation, fault analysis, and advanced controls to manage fault performance of inverters.

We review related prior literature focusing on the following.

1) Efforts where three-phase networks are realized with single-phase inverter-based resources.
2) Stability of phase-angle dynamics in the context of power electronics.
3) Aggregation of inverter dynamics.

Majority of existing research on multi-inverter systems is focused on three- (or single-) phase systems built exclusively with three- (or single-) phase inverters. Such approaches overlook the vision in Fig. 1. However, there are several notable exceptions. For instance, in [4], interphase static transfer switches are used to island a three-phase system with single-phase droop-controlled inverters. System-wide communications are used to manage the timing such that all three islanded ac phases are synchronized and then connected in parallel to form a larger single-phase island. Clearly such an approach requires nontrivial modifications to the network, entails additional hardware, and cannot provide power to three-phase loads. There is another line of related work where microgrids are assembled using a mix of three- and single-phase inverters [5], [6]. In such settings, three-phase inverters innately ensure phase balancing at the outset and single-phase inverters hang off of each phase. Such an approach skirts the challenges of obtaining a balanced three-phase system purely with single-phase generation. A recent work that is closely related is [7]; in here, a hybrid system model containing three- and single-phase GFM inverters across transmission and distribution is examined. A method to characterize small-signal stability of the inverter-based system is put forward using a linearized power flow model that accommodates imbalances and various transformer interconnection types (e.g., wye-delta and wye-wye). By and large, stability assessment, as it pertains to GFM technology, is a very active area of research, and we point interested readers to the survey effort in [8] for detailed discussions of contemporary efforts. While stability of phase-difference dynamics in the context of GFM technology—our particular focus in this effort—is not widely studied, it has received attention in the context of switch interleaving in dc–dc converters [9]. Theoretical results covering stability of phase-difference dynamics are also available for networks of Van der Pol oscillators [10], Liénard-type oscillators [11], and planar particles moving at constant speed [12], [13]. Finally, we point out that our effort also contributes to aggregation of inverter models at the intersection of three-phase power-system analysis

and power-electronics circuits, factoring in transformer characteristics. In general, aggregation is an active research area and there has been significant contemporary interest in development of aggregate inverter models for different inverter-control types (e.g., grid-following [14] and grid-forming (GFM) [15]), and applications (e.g., PV [16] and wind [17]).

To summarize, in the context of the literature surveyed above, this article provides the following contributions.

1) Resilient operation of three-phase power networks with single-phase power-electronics circuits.
2) Large-signal stability assessment of the phase-difference dynamics of nonlinear oscillators.
3) Modeling of aggregations of inverter dynamics across multiple phases including transformer interconnections.

Taken together, it paves the way for ultraresilient distribution systems by outlining an analytical framework (supported by experiments) for phase-balanced operation.

The rest of this article is organized as follows. In Section II, we describe the system models focusing on the GFM inverters, transformers, and their interconnection. Section III focuses on the derivation of two equivalent-circuit aggregate models: for inverters connected in each phase and for the entire distribution network encompassing all three phases. Building on this model, we obtain the dynamical model that governs the phase-angle differences for aggregates in Section IV. This section also puts forth the main analytical contribution of the work, i.e., large-signal stability assessment of the phase-balanced equilibria. Next, Section V provides experimental validation to support the analytical developments and demonstrates the robustness of the overall strategy. Finally, Section VI concludes this article.

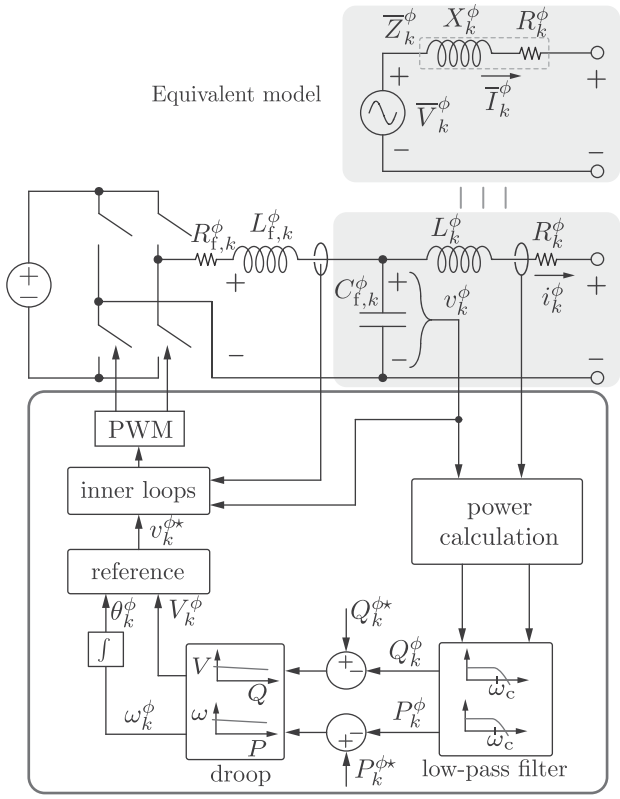

Fig. 3. Up-close look at the kth inverter in phase ϕ with droop control implemented for GFM operation. An equivalent model at the capacitive filter terminals comprising a controlled voltage source is presumed for analytical developments that follow.

II. System Description and Modeling

In this section, we provide an overview of all constituent models that make up the system architecture in Fig. 2(a). We begin with notation, then move on to the model for individual single-phase droop-controlled inverters, and finally, discuss the transformer model that interconnects them.

A. Notation and System-Architecture Overview

Referring to Fig. 2(a), the low-voltage primary side of the power transformer has clusters of single-phase GFM voltage source inverters distributed across its phases. Distribution systems are realized with a multitude of transformers that convert between various voltage levels and with a mix of wiring schemes. We zoom in on an elemental subsystem comprising a single transformer with single-phase resources on the low-voltage wye-connected side and the high-voltage delta-connected side is interfaced with the remainder of the transmission network. All inverters have the same nominal voltage and frequency ratings, i.e., $V_{\rm nom}$ and $\omega_{\rm nom}$. The number of inverters on phases a, b, and c are denoted by $n_{\rm a}$, $n_{\rm b}$, and $n_{\rm c}$, respectively; and S_k^ϕ ($k \in \{1, \ldots, n_\phi\}$) denotes the apparent power rating of the kth inverter on phase $\phi \in \Phi = \{{\rm a}, {\rm b}, {\rm c}\}$. While individual inverters may have different nameplate capacities, the aggregate ratings of all inverters across the phases are assumed to be the same

$$\sum_{k=1}^{n_{\rm a}} S_k^{\rm a} = \sum_{k=1}^{n_{\rm b}} S_k^{\rm b} = \sum_{k=1}^{n_{\rm c}} S_k^{\rm c} =: S. \tag{1}$$

The bus-voltage magnitude and phase angle on phase ϕ are denoted by V^ϕ and θ^ϕ; $\overline{Z}_{\rm load}$ denotes the local-load impedance on each phase while $\overline{Z}_{\rm load,s}$ is the load impedance on the high-voltage secondary side. Note that the loads on the primary and secondary sides of the transformers are all assumed to be identical; in other words, the distribution network is assumed to be balanced with regard to the aggregate load.

B. GFM Control Implementation

The structure of an individual GFM inverter and its controller implementation are shown in Fig. 3. Each inverter is fed by a dc voltage source and the power stage performs dc–ac conversion where the ac output features an LCL filter. The capacitive branch of the kth LCL filter on phase ϕ presents instantaneous voltage

$$v_k^\phi = \sqrt{2}\, V_k^\phi \cos\theta_k^\phi \tag{2}$$

where V_k^ϕ is the RMS amplitude, $\theta_k^\phi = \int \omega_k^\phi(\tau){\rm d}\tau$ is the phase angle, and the corresponding angular frequency is denoted by ω_k^ϕ. In phasor form, (2) reads $\overline{V}_k^\phi = V_k^\phi \angle \theta_k^\phi$. As shown at the top of Fig. 3, the inverter is modeled as an equivalent voltage

source, $\overline{V}_k^{\phi}$, with an RL output impedance, $\overline{Z}_k^{\phi} = R_k^{\phi} + \jmath X_k^{\phi}$, that includes the effect of its filter. We assume the following.

Assumption 1: Inverter output impedances are identical when perunitized in their own bases. In particular $\forall i \in \{1, \ldots, n_\phi\}, j \in \{1, \ldots, n_{\phi'}\}$, and $\phi, \phi' \in \Phi$

$$R_{\text{pu}} = \frac{R_i^{\phi}}{Z_{\text{base},i}^{\phi}} = \frac{R_j^{\phi'}}{Z_{\text{base},j}^{\phi'}}, \; X_{\text{pu}} = \frac{X_i^{\phi}}{Z_{\text{base},i}^{\phi}} = \frac{X_j^{\phi'}}{Z_{\text{base},j}^{\phi'}} \tag{3}$$

where R_{pu} and X_{pu} denote the perunit resistance and reactance, and the inverter base impedances are given by

$$Z_{\text{base},k}^{\phi} = \frac{V_{\text{nom}}^2}{S_k^{\phi}}.$$

Each inverter contains a set of independent control loops shown within the inset at the bottom of Fig. 3. Inner control loops ensure that the voltage v_k^{ϕ} closely tracks the reference $v_k^{\phi\star}$ generated by the outer droop controller. The voltage and frequency droop relations are

$$V_k^{\phi} = V_{\text{nom}} - m_{\text{q}k}^{\phi}\left(Q_k^{\phi} - Q_k^{\phi\star}\right) \tag{4a}$$

$$\omega_k^{\phi} = \omega_{\text{nom}} - m_{\text{p}k}^{\phi}\left(P_k^{\phi} - P_k^{\phi\star}\right) \tag{4b}$$

where V_{nom}, ω_{nom} are the nominal grid voltage and frequency; $m_{\text{q}k}^{\phi}$ and $m_{\text{p}k}^{\phi}$ are voltage- and frequency-droop slopes; P_k^{ϕ} and Q_k^{ϕ} are filtered active- and reactive-power output-terminal measurements; and $P_k^{\phi\star}$ and $Q_k^{\phi\star}$ are active- and reactive-power references. Note from Fig. 3 that a low-pass filter is assumed to be implemented to eliminate double-frequency fluctuations from the power calculations. The bandwidth of this filter, ω_{c}, ranges from several Hz to tens of Hz for typical single-phase applications [18], [19].

Systematic selection of inverter droop slopes $m_{\text{q}k}^{\phi}$ and $m_{\text{p}k}^{\phi}$ ensures power sharing among inverters in proportion to their nameplate capacities. Denote the specifications on voltage and frequency deviations by $\Delta V_{\max}$ and $\Delta\omega_{\max}$, respectively. We make the following assumption on design of the droop slopes.

Assumption 2: Inverters across the system are tuned for identical deviations in voltage and frequency. In particular $\forall k \in \{1, \ldots, n_\phi\}, \phi \in \Phi$, we have

$$m_{\text{q}k}^{\phi}\, S_k^{\phi} = \Delta V_{\max} \tag{5a}$$

$$m_{\text{p}k}^{\phi}\, S_k^{\phi} = \Delta\omega_{\max}. \tag{5b}$$

Notice that (5) can be implemented in a decentralized fashion.

The primary objective of GFM control, (such as droop control discussed above) is to yield frequency synchronization. A wide body of work has investigated precise necessary and sufficient conditions based on network and device control parameters for frequency synchronization. We point to the results in, e.g., [20] and [21] that can be leveraged to prove frequency synchronization in each phase. In what follows, we make the following assumption.

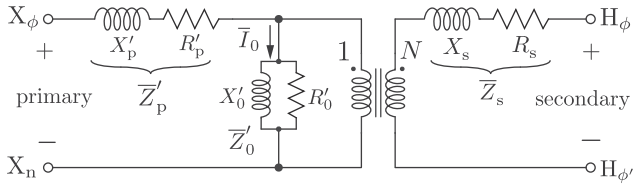

Fig. 4. Illustration of the transformer equivalent-circuit models. The perphase equivalent circuit capturing the wye-connected primary and delta-connected secondary is shown in (a), the equivalent circuit with all impedances reflected to the secondary is shown in (b).

Assumption 3: Inverters in each phase are frequency synchronized, i.e.,

$$\omega_i^{\phi} = \omega_j^{\phi} = \omega^{\phi} \qquad \forall i, j \in \{1, \ldots, n_\phi\} \tag{6}$$

where ω^{ϕ} is the common frequency on phase $\phi \in \Phi$.

The phenomenon of collocated inverters oscillating with the same (fundamental) frequency resonates with the notion of coherency, that has found extensive mention in the modeling, analysis, and control of collective dynamics of energy-conversion interfaces including synchronous generators [22], GFM inverters [15], and grid-following inverters [14]. Without Assumption 3, we are faced with the prospect of analyzing a higher-order dynamical system (with order approaching the number of inverters). This induces several analytical bottlenecks and limits the possibility of inferring general trends and results, such as the ones we converge upon via theoretical analysis.

We do not dwell on details on system-level controllers and the manner in which setpoints $P_k^{\phi\star}, Q_k^{\phi\star}$ are synthesized. However, to ensure fairness of participation in system-level control, we suppose these setpoints are issued to be equal in a per-unit sense. In particular $\forall i \in \{1, \ldots, n_\phi\}, j \in \{1, \ldots, n_{\phi'}\}$ and $\phi, \phi' \in \Phi$, we have

$$\frac{P_i^{\phi\star}}{S_i^{\phi}} = \frac{P_j^{\phi'\star}}{S_j^{\phi'}}, \quad \frac{Q_i^{\phi\star}}{S_i^{\phi}} = \frac{Q_j^{\phi'\star}}{S_j^{\phi'}}. \tag{7}$$

C. Transformers and Equivalent-Circuit Representation

The wye-connected primary and delta-connected secondary windings of the transformer are modeled with the prototypical per-phase equivalent circuit in Fig. 4. The model includes leakage and magnetizing impedances as well as an ideal transformer with turns ratio N. Primary- and secondary-side leakage impedances are denoted by $\overline{Z}'_{\text{p}} = R'_{\text{p}} + \jmath X'_{\text{p}}$ and $\overline{Z}_{\text{s}} = R_{\text{s}} + \jmath X_{\text{s}}$, respectively. The magnetizing current, $\overline{I}_0$, flows through the magnetizing impedance, $\overline{Z}'_0 = R'_0 \,\|\, \jmath X'_0$. Impedances reflected to the high-voltage secondary side are denoted $\overline{Z}_{\text{p}} = N^2\overline{Z}'_{\text{p}}$ and $\overline{Z}_0 = N^2\overline{Z}'_0$.

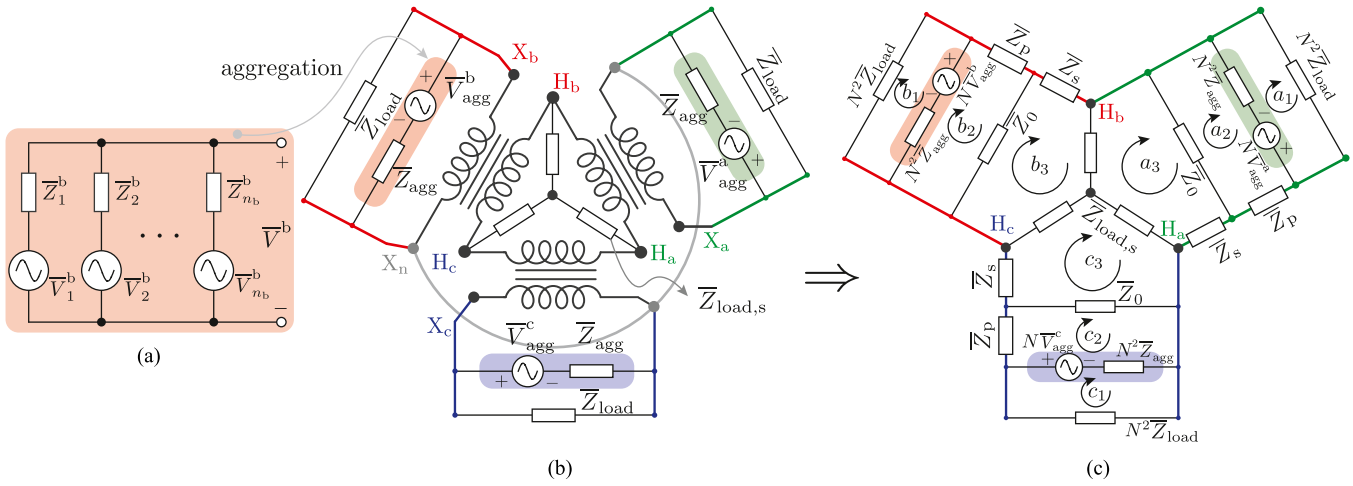

Fig. 5. Interconnected single-phase GFM inverters with a three-phase wye-delta transformer: (a) Per-phase equivalent representation of parallel inverters. (b) Equivalent-circuit network model with aggregated GFM inverter models. (c) Equivalent-circuit model with all elements reflected to high-voltage side of the transformer. Note that (c) is equivalent to the circuit in Fig. 2(b); see discussion surrounding (42) in Appendix B.

III. Per-Phase Aggregation and Equivalent-Circuit Network Model

In this section, we present: 1) an equivalent-circuit aggregate model for the inverters dispersed across an individual phase [see Fig. 5(a) and (b)], and 2) an equivalent-circuit model for the entire network with all resources (inverters and loads) reflected to the high-voltage-terminals of the transformers [see Fig. 5(c), or equivalently, Fig. 2(b)]. Our motivation in pursuing these is to leverage the equivalent-circuit network model to obtain the dynamics for phase differences of aggregates of inverters.

A. Equivalent-Circuit Per-Phase Aggregate Model

Denoting the bus voltage phasor as $\overline{V}^{\phi} = V^{\phi}\angle\theta^{\phi}$ (see Fig. 5), we can obtain the power-flow equations of the kth inverter in phase $\phi \in \Phi$ as

$$\begin{bmatrix} P_k^{\phi} \\ Q_k^{\phi} \end{bmatrix} = \frac{V^{\phi}}{Z_k^{\phi}} \begin{bmatrix} \cos\varphi_k^{\phi} & \sin\varphi_k^{\phi} \\ \sin\varphi_k^{\phi} & -\cos\varphi_k^{\phi} \end{bmatrix} \begin{bmatrix} V_k^{\phi}\cos(\theta_k^{\phi}-\theta^{\phi}) - V^{\phi} \\ V_k^{\phi}\sin(\theta_k^{\phi}-\theta^{\phi}) \end{bmatrix} \tag{8}$$

where $\varphi_k^{\phi} = \arctan(X_k^{\phi}/R_k^{\phi})$ is the impedance angle corresponding to the output impedance of the kth inverter. To facilitate analysis, we suppose that the phase difference between the filter–capacitor voltage of each inverter and the bus voltage is small, i.e., $\theta_k^{\phi} - \theta^{\phi} \approx 0$; this invites the following linearization for trigonometric terms appearing in the power-flow expressions above

$$\sin(\theta_k^{\phi} - \theta^{\phi}) \approx \theta_k^{\phi} - \theta^{\phi}, \quad \cos(\theta_k^{\phi} - \theta^{\phi}) \approx 1.$$

Consequently, with some algebraic manipulations, (8) yields

$$V_k^{\phi} = V^{\phi} + \frac{R_k^{\phi}P_k^{\phi} + X_k^{\phi}Q_k^{\phi}}{V^{\phi}} \tag{9a}$$

$$\theta_k^{\phi} = \theta^{\phi} + \frac{X_k^{\phi}P_k^{\phi} - R_k^{\phi}Q_k^{\phi}}{V^{\phi}V_k^{\phi}}. \tag{9b}$$

With the aid of (3) and (5), we can express (9a)–(9b) as

$$V_k^{\phi} = V^{\phi} + V_{\text{nom}}^2 \frac{R_{\text{pu}}\left(\frac{P_k^{\phi}}{S_k^{\phi}}\right) + X_{\text{pu}}\left(\frac{Q_k^{\phi}}{S_k^{\phi}}\right)}{V^{\phi}} \tag{10a}$$

$$\theta_k^{\phi} = \theta^{\phi} + V_{\text{nom}}^2 \frac{X_{\text{pu}}\left(\frac{P_k^{\phi}}{S_k^{\phi}}\right) - R_{\text{pu}}\left(\frac{Q_k^{\phi}}{S_k^{\phi}}\right)}{V^{\phi}V_k^{\phi}}. \tag{10b}$$

With the aid of these expressions, we can establish power sharing. In particular

$$\frac{P_1^{\phi}}{S_1^{\phi}} = \frac{P_2^{\phi}}{S_2^{\phi}} = \cdots = \frac{P_{n_{\phi}}^{\phi}}{S_{n_{\phi}}^{\phi}} = \frac{P^{\phi}}{S} \tag{11a}$$

$$\frac{Q_1^{\phi}}{S_1^{\phi}} = \frac{Q_2^{\phi}}{S_2^{\phi}} = \cdots = \frac{Q_{n_{\phi}}^{\phi}}{S_{n_{\phi}}^{\phi}} = \frac{Q^{\phi}}{S} \tag{11b}$$

where S is defined in (1), and we introduce the aggregate reactive and active powers generated per phase as

$$Q^{\phi} = \sum_{k=1}^{n_{\phi}} Q_k^{\phi}, \quad P^{\phi} = \sum_{k=1}^{n_{\phi}} P_k^{\phi}. \tag{12}$$

See Appendix A for a proof to (11). With the aid of (11), we see from (10) that voltages and phase angles are identical for all inverters on the branch. In particular

$$V_k^{\phi} = V_{\text{agg}}^{\phi}, \quad \theta_k^{\phi} = \theta_j^{\phi} \tag{13}$$

with V_{agg}^{ϕ} denoting the common voltage amplitude. This observation allows us to aggregate the parallel inverters; see Fig. 5(a) and (b). Inspection of this circuit allows us to compute the equivalent per-phase output impedance as

$$\overline{Z}_{\text{agg}} = \overline{Z}_1^{\phi} \parallel \overline{Z}_2^{\phi} \parallel \ldots \parallel \overline{Z}_{n_{\phi}}^{\phi} = \frac{V_{\text{nom}}^2}{S}(R_{\text{pu}} + \jmath X_{\text{pu}}). \tag{14}$$

With the aid of (4a), (13), and the reactive power-sharing equation in (11b), we can get the following aggregated voltage-droop

equation:

$$V_{\text{agg}}^{\phi} = V_{\text{nom}} - \Delta V_{\max}\left(\frac{Q^{\phi}}{S} - \frac{Q^{\phi\star}}{S}\right) = V_{\text{nom}} - m_{\text{q}}\left(Q^{\phi} - Q^{\phi\star}\right) \tag{15}$$

where $m_{\text{q}} = \frac{\Delta V_{\max}}{S}$, $Q^{\phi} = \sum_{k=1}^{n_{\phi}} Q_k^{\phi}$, and $Q^{\phi\star} = \sum_{k=1}^{n_{\phi}} Q_k^{\phi\star}$. Similarly, combining (38) and the active power-sharing equation in (11a), we obtain the following aggregated frequency-droop equation:

$$\omega^{\phi} = \omega_{\text{nom}} - \Delta\omega_{\max}\left(\frac{P^{\phi}}{S} - \frac{P^{\phi\star}}{S}\right) = \omega_{\text{nom}} - m_{\text{p}}\left(P^{\phi} - P^{\phi\star}\right) \tag{16}$$

where $m_{\text{p}} = \frac{\Delta\omega_{\max}}{S}$, $P^{\phi} = \sum_{k=1}^{n_{\phi}} P_k^{\phi}$, and $P^{\phi\star} = \sum_{k=1}^{n_{\phi}} P_k^{\phi\star}$.

We note that aggregation of inverter dynamics is an active area of research. While we begin with the simplified equivalent model of a controlled voltage source behind a reactance for individual inverters, other efforts that dwell singularly on aggregation have focused on retaining the impact of inner-loop dynamics, see, e.g., [23].

B. Equivalent-Circuit Network Model

The aggregated inverter equivalent in tandem with a wye-delta transformer gives the system in Fig. 5(b) where phasors $\overline{V}_{\text{agg}}^{\phi}$ and $\overline{Z}_{\text{agg}}$ represent the phase ϕ aggregated inverter. Application of the transformer model in Fig. 4 and reflecting all circuit elements to the secondary side gives the equivalent circuit in Fig. 5(c). Since our goal is to model inverter phase dynamics, and particularly, their interaction across phases, it is necessary to compute the active power flowing through the three branches, which contain aggregated inverter equivalents.

Utilizing a suite of circuit-theoretic constructs and power-flow analysis, we can extract the active and reactive powers (real and imaginary parts of $\overline{S}^{\phi}$) generated by the phase ϕ aggregated inverter model as

$$P^{\phi} = \sum_{k\in\Phi} \frac{N^2\, V_{\text{agg}}^{k} V_{\text{agg}}^{\phi} \cos\left(\theta^{k\phi} - \varphi_1\right)}{Z_{\text{eq1}}} + P_{\text{load}}^{\phi} \tag{17a}$$

$$Q^{\phi} = -\sum_{k\in\Phi} \frac{N^2\, V_{\text{agg}}^{k} V_{\text{agg}}^{\phi} \sin\left(\theta^{k\phi} - \varphi_1\right)}{Z_{\text{eq1}}} + Q_{\text{load}}^{\phi} \tag{17b}$$

where $\theta^{k\phi} = \theta^{k} - \theta^{\phi}$ is the angle difference of aggregated inverters on phase k and ϕ, P_{load}^{ϕ} and Q_{load}^{ϕ} are the total active and reactive power in the loads (including losses)

$$P_{\text{load}}^{\phi} = \frac{(NV_{\text{agg}}^{\phi})^2}{Z_{\text{eq2}}}\cos\varphi_2,\quad Q_{\text{load}}^{\phi} = -\frac{(NV_{\text{agg}}^{\phi})^2}{Z_{\text{eq2}}}\sin\varphi_2 \tag{18}$$

and $\overline{Z}_{\text{eq1}} = Z_{\text{eq1}}\angle\varphi_1$, $\overline{Z}_{\text{eq2}} = Z_{\text{eq2}}\angle\varphi_2$ are equivalent impedances. Appendix C provides a sketch of the derivation to (17), and closed-form expressions for $\overline{Z}_{\text{eq1}}$ and $\overline{Z}_{\text{eq2}}$. In fact, the same derivation, particularly the representation of phase currents in (42), invites the equivalent-circuit representation in Fig. 2(b), as well as establishes the equivalence of Figs. 2(b) and 5(c).

The assumption on small angle differences utilized when deriving the equivalent aggregate model of the single-phase inverters is applied for each *individual* phase. Note that we do not assume the angle differences *between* phases is small and retain the large-signal nonlinear impacts in the overall three-phase system. This explains why the model in (17) includes nonlinear trigonometric terms. To summarize, we assume intraphase angle differences are small, but we do not suppose anything similar for the interphase angle differences.

Next, we integrate the active and reactive power expressions above with the droop laws that govern the dynamics of the aggregated inverter equivalents. Since P^{ϕ} and Q^{ϕ} in (17) are steady-state values, they are numerically equal to the average power measurements in (15) and (16). Therefore, substitution of (17) into (15) and (16) with the further assumption that $P^{\phi\star} = P_{\text{load}}^{\phi}$ and $Q^{\phi\star} = Q_{\text{load}}^{\phi}$ yields

$$V_{\text{agg}}^{\phi} = V_{\text{nom}} + m_{\text{q}} \sum_{k\in\Phi} \frac{N^2\, V_{\text{agg}}^{k} V_{\text{agg}}^{\phi}}{Z_{\text{eq1}}} \sin\left(\theta^{k\phi} - \varphi_1\right) \tag{19a}$$

$$\dot{\theta}^{\phi} = \omega_{\text{nom}} - m_{\text{p}} \sum_{k\in\Phi} \frac{N^2\, V_{\text{agg}}^{k} V_{\text{agg}}^{\phi}}{Z_{\text{eq1}}} \cos\left(\theta^{k\phi} - \varphi_1\right). \tag{19b}$$

The leading assumption implies that inverters are dispatched by a secondary controller that restores voltage and frequency to nominal values (by driving $P^{\phi\star} \to P_{\text{load}}^{\phi}$ and $Q^{\phi\star} \to Q_{\text{load}}^{\phi}$).

In general, the transformer magnetizing impedance, $\overline{Z}_0$, and load impedances, $\overline{Z}_{\text{load}}$ and $\overline{Z}_{\text{load,s}}$, are much larger than transformer leakage impedances, $\overline{Z}_{\text{p}}$ and $\overline{Z}_{\text{s}}$, and inverter output impedance, $\overline{Z}_{\text{agg}}$, i.e., $\overline{Z}_0 \gg \overline{Z}_{\text{p}}, \overline{Z}_{\text{s}}, \overline{Z}_{\text{agg}}$ and $\overline{Z}_{\text{load}}, \overline{Z}_{\text{load,s}} \gg \overline{Z}_{\text{p}}, \overline{Z}_{\text{s}}, \overline{Z}_{\text{agg}}$. Applying these to the expressions for $\overline{Z}_{\text{eq1}}$ and $\overline{Z}_{\text{eq2}}$ in (43) (see Appendix B), we can get the following approximations:

$$\overline{Z}_{\text{eq1}} \approx 3(N^2\overline{Z}_{\text{agg}} + \overline{Z}_{\text{p}} + \overline{Z}_{\text{s}}) \tag{20a}$$

$$\overline{Z}_{\text{eq2}} \approx \frac{3\overline{Z}_{\text{load,s}}(N^2\overline{Z}_{\text{load}})}{3\overline{Z}_{\text{load,s}} + N^2\overline{Z}_{\text{load}}}. \tag{20b}$$

We observe that $\overline{Z}_{\text{eq1}}$ is dominantly related to the inverter and transformer impedances, but not the secondary loads; similarly, $\overline{Z}_{\text{eq2}}$ is dominantly related to the primary and secondary loads. Under common practice, the inverter output impedance and the transformer windings are expected to be dominantly inductive. As a result, $\varphi_1 \approx \frac{\pi}{2}$. Consequently, (19) simplifies to

$$V_{\text{agg}}^{\phi} = V_{\text{nom}} - m_{\text{q}} \sum_{k\in\Phi} \frac{N^2\, V_{\text{agg}}^{k} V_{\text{agg}}^{\phi}}{Z_{\text{eq1}}} \cos\theta^{k\phi} \tag{21a}$$

$$\dot{\theta}^{\phi} = \omega_{\text{nom}} - m_{\text{p}} \sum_{k\in\Phi} \frac{N^2\, V_{\text{agg}}^{k} V_{\text{agg}}^{\phi}}{Z_{\text{eq1}}} \sin\theta^{k\phi}. \tag{21b}$$

Notably, (21b) is a Kuramoto-type model. Several instances have been documented of such Kuramoto-type dynamical models appearing in the analysis of GFM inverters, see, e.g., [21], [24].

IV. Phase-Balanced Operation

In this section, we first leverage the model in (21) to derive the dynamics that govern the phase differences. Next, we characterize (in)stability of the identified equilibria. As the main result, we show that phase-balanced equilibria are asymptotically stable and identify an ROA for them. For this, we leverage Lyapunov stability theory [25].

A. Phase-Difference Dynamics and Equilibria

Pick phase-a angle, θ^{a}, as a reference. Define $\theta^{\mathrm{ba}} = \theta^{\mathrm{b}} - \theta^{\mathrm{a}}$ and $\theta^{\mathrm{ca}} = \theta^{\mathrm{c}} - \theta^{\mathrm{a}}$. From (21b), we get the following:

$$\dot{\theta}^{\mathrm{ba}} = \frac{m_{\mathrm{p}} N^2}{Z_{\mathrm{eq1}}} \left(V^{\mathrm{b}}_{\mathrm{agg}} V^{\mathrm{a}}_{\mathrm{agg}} \sin\theta^{\mathrm{ba}} + V^{\mathrm{c}}_{\mathrm{agg}} V^{\mathrm{a}}_{\mathrm{agg}} \sin\theta^{\mathrm{ca}} - V^{\mathrm{c}}_{\mathrm{agg}} V^{\mathrm{b}}_{\mathrm{agg}} \sin\theta^{\mathrm{cb}} - V^{\mathrm{b}}_{\mathrm{agg}} V^{\mathrm{a}}_{\mathrm{agg}} \sin\theta^{\mathrm{ab}} \right) \tag{22a}$$

$$\dot{\theta}^{\mathrm{ca}} = \frac{m_{\mathrm{p}} N^2}{Z_{\mathrm{eq1}}} \left(V^{\mathrm{c}}_{\mathrm{agg}} V^{\mathrm{a}}_{\mathrm{agg}} \sin\theta^{\mathrm{ca}} + V^{\mathrm{b}}_{\mathrm{agg}} V^{\mathrm{a}}_{\mathrm{agg}} \sin\theta^{\mathrm{ba}} - V^{\mathrm{c}}_{\mathrm{agg}} V^{\mathrm{b}}_{\mathrm{agg}} \sin\theta^{\mathrm{bc}} - V^{\mathrm{a}}_{\mathrm{agg}} V^{\mathrm{c}}_{\mathrm{agg}} \sin\theta^{\mathrm{ac}} \right). \tag{22b}$$

Substituting instances of V^{ϕ}_{agg} from (19a) into the expressions above and ignoring product terms $m_{\mathrm{p}} m_{\mathrm{q}}^2$ and $m_{\mathrm{p}} m_{\mathrm{q}}$, we get

$$\dot{\theta}^{\mathrm{ba}} = K \left(2\sin\theta^{\mathrm{ba}} + \sin\theta^{\mathrm{ca}} + \sin\left(\theta^{\mathrm{ba}} - \theta^{\mathrm{ca}}\right) \right) \tag{23a}$$

$$\dot{\theta}^{\mathrm{ca}} = K \left(2\sin\theta^{\mathrm{ca}} + \sin\theta^{\mathrm{ba}} + \sin\left(\theta^{\mathrm{ca}} - \theta^{\mathrm{ba}}\right) \right) \tag{23b}$$

where $K = \frac{m_{\mathrm{p}} N^2 V^2_{\mathrm{nom}}}{Z_{\mathrm{eq1}}}$. Denote the equilibria of (23) by $\theta^{\mathrm{ba}}_{\mathrm{eq}}$ and $\theta^{\mathrm{ca}}_{\mathrm{eq}}$. The following equilibria are obtained by setting $\dot{\theta}^{\mathrm{ba}} = 0$ and $\dot{\theta}^{\mathrm{ca}} = 0$ and solving the ensuing algebraic equations:

$$\left(\theta^{\mathrm{ba}}_{\mathrm{eq}},\ \theta^{\mathrm{ca}}_{\mathrm{eq}}\right) \in \{ \left(\tfrac{2\pi}{3},\ \tfrac{4\pi}{3}\right),\ \left(\tfrac{4\pi}{3},\ \tfrac{2\pi}{3}\right),\ (0,0) \\ (0,\pi),\ (\pi,0),\ (\pi,\pi) \}. \tag{24}$$

In addition to the phase-balanced equilibria $(\frac{2\pi}{3},\ \frac{4\pi}{3})$, $(\frac{4\pi}{3},\ \frac{2\pi}{3})$, we note other equilibria $(0,0), (0,\pi), (\pi,0), (\pi,\pi)$. Next, we characterize the stability of all the equilibria listed above. Before doing so, we present some mathematical preliminaries.

B. Mathematical Preliminaries

Consider the autonomous dynamical system $\dot{x} = f(x)$ where $f : \mathcal{D} \to \mathbb{R}^n$ is a locally Lipschitz map from domain $\mathcal{D} \subset \mathbb{R}^n$ into $\mathbb{R}^n$. Denote the equilibrium point(s) of the system—defined as solutions of algebraic equations $f(x) = 0$—by x_{eq}. Denote the trajectory generated by the system at time t emanating from initial condition $x_\circ$ (corresponding to time $t_\circ$) by $x(t, x_\circ)$.

First, we introduce the notion of a *positively invariant set*. We will find this useful in characterizing the ROA of stable equilibria.

Definition 1 (Positively Invariant Set): A set Ω is said to be **positively invariant** if

$$x_\circ \in \Omega \Longrightarrow x(t, x_\circ) \in \Omega \quad \forall t \geq t_\circ.$$

A sufficient condition to guarantee positive invariance of Ω is

$$\dot{x} \cdot \eta < 0 \qquad \forall x \in \partial\Omega \tag{25}$$

where η is the outward normal on the boundary $\partial\Omega$ of Ω. Satisfying (25) ensures every trajectory flow that arrives at the boundary would flow into the interior of the set.

Definition 2 (Region of Attraction): The ROA of the dynamical system for a stable equilibrium point, x_{eq}, is denoted by $\mathcal{R}(x_{\mathrm{eq}})$ and defined as

$$\mathcal{R}(x_{\mathrm{eq}}) = \left\{ x_\circ \in \mathbb{R}^n \mid \lim_{t\to\infty} x(t, x_\circ) = x_{\mathrm{eq}} \right\}. \tag{26}$$

By definition, the ROA is a connected set.

Theorem 1 (Lyapunov Theorem for Local Stability): Let $V : \mathcal{D} \to \mathbb{R}$ be a continuously differentiable Lyapunov function that satisfies

$$V(x_{\mathrm{eq}}) = 0 \ \text{ and } \ V(x) > 0, \dot{V}(x) < 0 \quad \forall x \in \mathcal{D} \setminus x_{\mathrm{eq}}. \tag{27}$$

Then, x_{eq} is asymptotically stable.

For a Lyapunov function, V, that satisfies the conditions of asymptotic stability over domain $\mathcal{D}$, any compact positively invariant set $\Omega \subset \mathcal{D}$ is a subset of the ROA, $\mathcal{R}(x_{\mathrm{eq}})$. In particular, all trajectories emanating from points inside Ω will converge to the asymptotically stable equilibrium point, x_{eq}.

The definitions thus far (implicitly) focus on stable equilibria. Indeed, we also contend with unstable equilibria and saddle points in the investigated dynamics. To characterize these, we consider the linearized model $\Delta\dot{x} = \mathcal{J}(x_{\mathrm{eq}})\Delta x$. Consider the 2-D case. If both eigenvalues of $\mathcal{J}(x_{\mathrm{eq}})$ have positive real parts, then x_{eq} is an unstable equilibrium. If, on the other hand, the two eigenvalues are real and of opposite signs, then x_{eq} is a saddle.

C. Stability Assessment of Phase-Balanced Equilibria

Recall that the phase-balanced equilibria are given by: $(\frac{2\pi}{3},\ \frac{4\pi}{3})$ and $(\frac{4\pi}{3},\ \frac{2\pi}{3})$. In what follows, we demonstrate that these are asymptotically stable and characterize their ROA.

1) Asymptotic Stability: Consider the candidate Lyapunov function

$$V(\theta^{\mathrm{ba}},\ \theta^{\mathrm{ca}}) = \frac{3}{2} - \cos\left(\theta^{\mathrm{ba}} - \frac{2\pi}{3}\right) - \cos\left(\theta^{\mathrm{ca}} - \frac{4\pi}{3}\right) - \cos\left(\theta^{\mathrm{ba}} - \frac{4\pi}{3}\right) - \cos\left(\theta^{\mathrm{ca}} - \frac{2\pi}{3}\right) - \cos\left(\theta^{\mathrm{ba}} - \theta^{\mathrm{ca}} + \frac{2\pi}{3}\right) - \cos\left(\theta^{\mathrm{ba}} - \theta^{\mathrm{ca}} - \frac{2\pi}{3}\right) \tag{28}$$

and the sets

$$\mathcal{D}_1 = \{(\theta^{\mathrm{ba}},\ \theta^{\mathrm{ca}}) \mid 0 < \theta^{\mathrm{ba}} < \theta^{\mathrm{ca}} < 2\pi\}$$

$$\mathcal{D}_2 = \{(\theta^{\mathrm{ba}},\ \theta^{\mathrm{ca}}) \mid 0 < \theta^{\mathrm{ca}} < \theta^{\mathrm{ba}} < 2\pi\}$$

$$\mathcal{D}_3 = \{(\theta^{\mathrm{ba}},\ \theta^{\mathrm{ca}}) \mid \theta^{\mathrm{ca}} = 0 \cup \theta^{\mathrm{ba}} = 0 \cup \theta^{\mathrm{ba}} = \theta^{\mathrm{ca}}\}. \tag{29}$$

Over domain $\mathcal{D}_1$ ($\mathcal{D}_2$, respectively), we see that $V(\theta^{\mathrm{ba}}, \theta^{\mathrm{ca}}) = 0$ if and only if $(\theta^{\mathrm{ba}},\ \theta^{\mathrm{ca}}) = (\frac{2\pi}{3},\ \frac{4\pi}{3})$ [$(\frac{4\pi}{3},\ \frac{2\pi}{3})$, respectively]. Furthermore, $V(\theta^{\mathrm{ba}}, \theta^{\mathrm{ca}}) > 0$ for all points in $\mathcal{D}_1, \mathcal{D}_2$ except the phase-balanced equilibria. [See Fig. 6(a).] Finally, we can

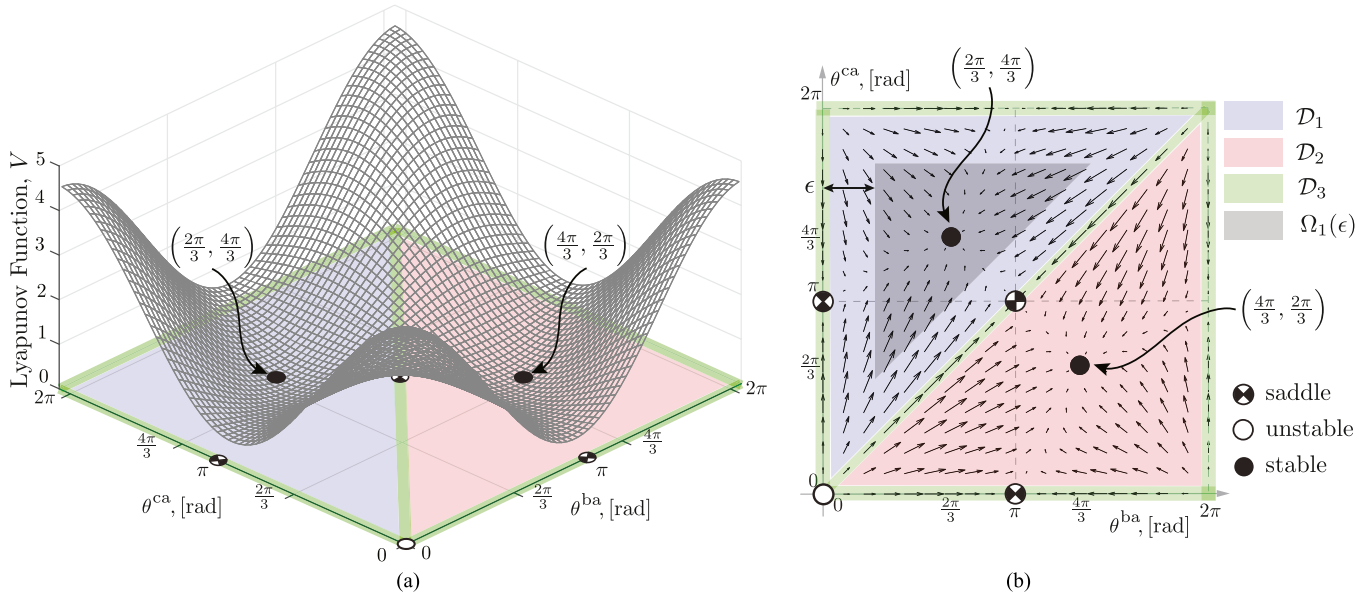

Fig. 6. (a) Lyapunov function V, which is clearly positive definite. Two local minima of the function are the stable equilibrium points. (b) Vector fields and all equilibria.

derive

$$\begin{aligned}\dot{V}(\theta^{ba}, \theta^{ca}) = &-\left(\sin\theta^{ba} + \sin\left(\theta^{ba} - \theta^{ca}\right)\right)^2 \\ &-\left(\sin\theta^{ca} + \sin\left(\theta^{ca} - \theta^{ba}\right)\right)^2 \\ &-\left(\sin\theta^{ba} + \sin\theta^{ca}\right)^2. \end{aligned} \tag{30}$$

We see that $\dot{V}(\theta^{ba}, \theta^{ca}) < 0$ for all points in $\mathcal{D}_1, \mathcal{D}_2$ except the phase-balanced equilibria. The function $V(\cdot,\cdot)$ satisfies all conditions laid out in Theorem 1; we can therefore establish the asymptotic stability of the phase-balanced equilibria.

2) Region of Attraction: Consider $\mathcal{R}(\frac{2\pi}{3}, \frac{4\pi}{3})$, the ROA corresponding to the equilibrium: $(\frac{2\pi}{3}, \frac{4\pi}{3})$. The first step to characterizing the ROA is to find a set contained in $\mathcal{D}_1$, which is positively invariant. Consider the candidate

$$\Omega_1(\epsilon) = \{(\theta^{ba}, \theta^{ca}) \mid 2\epsilon \le \theta^{ba} + \epsilon \le \theta^{ca} \le 2\pi - \epsilon\} \tag{31}$$

where $\epsilon \in (0, \frac{2\pi}{3})$. [See Fig. 6(b).] It can be proved that $\Omega_1(\epsilon)$ is a positively invariant set. To show this, we need to prove

$$(\dot{\theta}^{ba}, \dot{\theta}^{ca}) \cdot \eta < 0 \qquad \forall (\theta^{ba}, \theta^{ca}) \in \partial\Omega_1(\epsilon) \tag{32}$$

where η is the outward normal on the boundary $\partial\Omega_1(\epsilon)$ of the region $\Omega_1(\epsilon)$. From Fig. 6(b) we tease out three outward-normal vectors: $\eta_1 = (-1, 0)^{\mathrm{T}}$, $\eta_2 = (0, 1)^{\mathrm{T}}$, and $\eta_3 = (1, -1)^{\mathrm{T}}$ corresponding to the boundaries $\theta^{ba} = \epsilon$, $\theta^{ca} = 2\pi - \epsilon$, and $\theta^{ca} = \theta^{ba} + \epsilon$, respectively. We can boil down (32) for η_1, η_2, and η_3 to satisfying the following condition $\forall \epsilon \in (0, \frac{2\pi}{3}), \theta \in [0, 2\pi)$:

$$2\sin\epsilon + \sin\theta + \sin(\epsilon - \theta) > 0. \tag{33}$$

With the aid of elementary trigonometric identities, the left-hand side above can be factored as

$$2\sin\left(\frac{\epsilon}{2}\right)\left(2\cos\left(\frac{\epsilon}{2}\right) + \cos\left(\theta - \frac{\epsilon}{2}\right)\right).$$

For $\epsilon \in (0, \frac{2\pi}{3})$, $\sin(\frac{\epsilon}{2}) > 0$, and $\cos(\frac{\epsilon}{2}) > \frac{1}{2}$; from this, we see that (33) follows readily.

This above line of reasoning establishes $\Omega_1(\epsilon) \subset \mathcal{R}(\frac{2\pi}{3}, \frac{4\pi}{3})$. In fact, the determination also aids in establishing

$$\mathcal{D}_1 = \mathcal{R}\left(\frac{2\pi}{3}, \frac{4\pi}{3}\right). \tag{34}$$

We demonstrate this by proving $\mathcal{R}(\frac{2\pi}{3}, \frac{4\pi}{3}) \subset \mathcal{D}_1$ and $\mathcal{D}_1 \subset \mathcal{R}(\frac{2\pi}{3}, \frac{4\pi}{3})$; both by contradiction.

To show $\mathcal{D}_1 \subset \mathcal{R}(\frac{2\pi}{3}, \frac{4\pi}{3})$, we assume that there exists some (θ_1, θ_2) such that $(\theta_1, \theta_2) \in \mathcal{D}_1$ but $(\theta_1, \theta_2) \notin \mathcal{R}(\frac{2\pi}{3}, \frac{4\pi}{3})$. However, by construction, there always exists some ϵ such that $(\theta_1, \theta_2) \in \Omega_1(\epsilon) \subset \mathcal{R}(\frac{2\pi}{3}, \frac{4\pi}{3})$, thereby contradicting the fact that $\Omega_1(\epsilon) \subset \mathcal{D}_1$.

To show $\mathcal{R}(\frac{2\pi}{3}, \frac{4\pi}{3}) \subset \mathcal{D}_1$, consider that there exists some (θ_1, θ_2) such that $(\theta_1, \theta_2) \notin \mathcal{D}_1$ but $(\theta_1, \theta_2) \in \mathcal{R}(\frac{2\pi}{3}, \frac{4\pi}{3})$. Since $(\frac{2\pi}{3}, \frac{4\pi}{3}) \in \mathcal{D}_1$ and the ROA is a connected set, then any trajectory emanating from (θ_1, θ_2) to the equilibrium $(\frac{2\pi}{3}, \frac{4\pi}{3})$ intersects with $\partial\mathcal{D}_1$. Note, however, that $\partial\mathcal{D}_1 \subset \mathcal{D}_3$. Such an intersection contradicts the fact that no points in $\mathcal{D}_3$ are in $\mathcal{R}(\frac{2\pi}{3}, \frac{4\pi}{3})$, which can be derived from the facts that $(\frac{2\pi}{3}, \frac{4\pi}{3}) \notin \mathcal{D}_3$ and $\mathcal{D}_3$ is positively invariant. We close out the discussion by establishing the positive invariance for completeness. Since $\mathcal{D}_3 = \partial\mathcal{D}_3$, it suffices to satisfy the condition

$$(\dot{\theta}^{ba}, \dot{\theta}^{ca}) \cdot \zeta = 0 \qquad \forall (\theta^{ba}, \theta^{ca}) \in \mathcal{D}_3 \tag{35}$$

where ζ is the normal vector to the boundary of $\mathcal{D}_3$, to demonstrate the positive invariance of $\mathcal{D}_3$. From Fig. 6 we can identify three normal vectors, namely, $\zeta_1 = (1, 0)^{\mathrm{T}}$, $\zeta_2 = (0, 1)^{\mathrm{T}}$, and $\zeta_3 = (1, -1)^{\mathrm{T}}$ for boundaries $\theta^{ba} = 0$, $\theta^{ca} = 0$, and $\theta^{ca} = \theta^{ba}$, respectively. Evaluating the derivatives $(\dot{\theta}^{ba}, \dot{\theta}^{ca})$ at these boundaries, we obtain $(0, 3K\sin\theta^{ca})$, $(3K\sin\theta^{ba}, 0)$, and $(3K\sin\theta^{ba}, 3K\sin\theta^{ba})$, respectively. It can be verified that (35)

holds for all three cases. Thus, we conclude that $\mathcal{D}_3$ is positively invariant.

In a similar vein, we can establish

$$\mathcal{D}_2 = \mathcal{R}\left(\frac{4\pi}{3}, \frac{2\pi}{3}\right). \tag{36}$$

The discussion is not repeated in the interest of brevity.

D. Stability Assessment of Other Equilibria

Consider the other equilibria that we identify: $(0,0)$, $(0,\pi)$, $(\pi,0)$, (π,π). The small-signal model of the phase-difference dynamics (23) can be expressed as

$$\begin{bmatrix} \Delta\dot{\theta}^{\text{ba}} \\ \Delta\dot{\theta}^{\text{ca}} \end{bmatrix} = \mathcal{J}(\theta^{\text{ba}}_{\text{eq}}, \theta^{\text{ca}}_{\text{eq}}) \begin{bmatrix} \Delta\theta^{\text{ba}} \\ \Delta\theta^{\text{ca}} \end{bmatrix} \tag{37}$$

where $\Delta\theta^{\text{ba}}$, $\Delta\theta^{\text{ca}}$ denote small perturbations around the equilibria $(\theta^{\text{ba}}_{\text{eq}}, \theta^{\text{ca}}_{\text{eq}})$, and $\mathcal{J}(\theta^{\text{ba}}_{\text{eq}}, \theta^{\text{ca}}_{\text{eq}})$ is the Jacobian matrix given by

$$K \begin{bmatrix} 2\cos\theta^{\text{ba}}_{\text{eq}} + \cos(\theta^{\text{ba}}_{\text{eq}} - \theta^{\text{ca}}_{\text{eq}}) & \cos\theta^{\text{ca}}_{\text{eq}} - \cos(\theta^{\text{ba}}_{\text{eq}} - \theta^{\text{ca}}_{\text{eq}}) \\ \cos\theta^{\text{ba}}_{\text{eq}} - \cos(\theta^{\text{ca}}_{\text{eq}} - \theta^{\text{ba}}_{\text{eq}}) & 2\cos\theta^{\text{ca}}_{\text{eq}} + \cos(\theta^{\text{ca}}_{\text{eq}} - \theta^{\text{ba}}_{\text{eq}}) \end{bmatrix}.$$

Denote the eigenvalues of $\mathcal{J}(\theta^{\text{ba}}_{\text{eq}}, \theta^{\text{ca}}_{\text{eq}})$ by $\lambda_1(\theta^{\text{ba}}_{\text{eq}}, \theta^{\text{ca}}_{\text{eq}}), \lambda_2(\theta^{\text{ba}}_{\text{eq}}, \theta^{\text{ca}}_{\text{eq}})$. For the equilibria considered,

$$\lambda_1(0,0) = \lambda_2(0,0) = 3K > 0$$
$$\lambda_1(0,\pi) = \lambda_1(\pi,0) = \lambda_1(\pi,\pi) = K > 0$$
$$\lambda_2(0,\pi) = \lambda_2(\pi,0) = \lambda_2(\pi,\pi) = -3\,K < 0$$

establishing (0,0) to be unstable, and $(0,\pi), (\pi,0), (\pi,\pi)$ to be saddle points.

With the analytical developments discussed so far, we note that the ROA for the phase-balanced equilibria cover almost the entire phase plane. Therefore, it can be concluded that phase-balanced equilibria emergent in a system of interconnected single-phase GFM inverters are large-signal stable under balanced three-phase conditions.

V. Validation

In this section, we present numerical simulations and results from an experimental prototype to validate the analytical findings on stability of the phase-balanced equilibria. The numerical simulations focus on establishing robustness of the approach by considering asymmetric setups with disparity in values adopted for: droop slopes, load values, output impedances, and power setpoints. Nonlinear loads are also considered. On the other hand, the experimental setup focuses on overall evaluation in the face of large-signal disturbances including load changes and start-up from nonbalanced initial conditions.

A. System Description

The system considered for validation (simulations and experiments) consists of six single-phase GFM inverters with droop control connected across the three phases. A three-phase transformer with wye-delta connections is utilized and loads are included on both sides of the transformer. A schematic of the setup is shown in Fig. 7. Pertinent parameters are given in Table I. Note that these are applicable for both simulations and experiments.

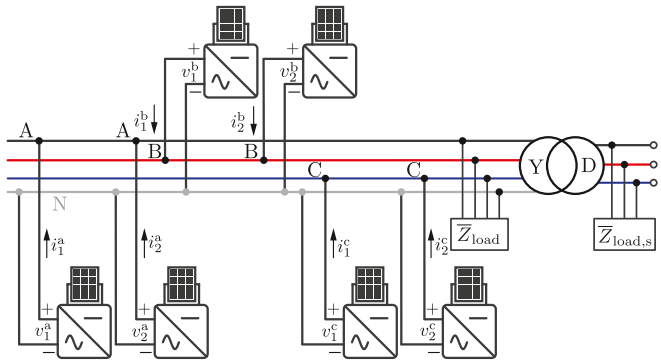

Fig. 7. Schematic of system utilized in the numerical simulations and experiments: six single-phase droop-controlled inverters, a transformer, and loads.

TABLE I
Parameters utilized in Numerical Simulations and Experimental Prototype

	Symbol	Description	Value	Units
Inverters	$n_{\text{a,b,c}}$	Units per phase	2	–
	S	Phase rating	1000	VA
	S/n_{a}	Inverter rating	500	VA
	V_{nom}	Nominal voltage	40	V_{rms}
	ω_{nom}	Nominal frequency	$60 \times 2\pi$	rad/s
	f_{sw}	Switching frequency	20	kHz
	L_{f}	Filter inductance	3	mH
	C_{f}	Filter capacitance	20	μF
	L	Filter inductance	0.94	mH
	R	Filter resistance	0.28	Ω
Transformer	-	Connection type	Y - Δ	-
	N	Turns ratio	$\frac{480}{120}$	-
	$\overline{Z}_{\text{p}}$	Primary impedance	$0.605 + \jmath 0.334$	Ω
	$\overline{Z}_{\text{s}}$	Secondary impedance	$0.605 + \jmath 0.334$	Ω
	$\overline{Z}_0$	Magnetizing impedance	$7.34 + \jmath 3.59$	kΩ
Loads	$\overline{Z}_{\text{load}}$	Local load	22	Ω
	$\overline{Z}_{\text{load,s}}$	Light secondary load	66	Ω
	$\overline{Z}_{\text{load,s}}$	Heavy secondary load	33	Ω
Controller	$\Delta\omega_{\text{max}}$	Frequency deviation	$0.5 \times 2\pi$	rad/s
	ΔV_{max}	Voltage deviation	$5\%V_{\text{nom}}$	V
	ω_{c}	LP filter bandwidth	$10 \times 2\pi$	rad/s
	m_{p}	Frequency droop	$\frac{0.5}{S}$	rad/(s·Var)
	m_{q}	Voltage droop	$\frac{5\%V_{\text{nom}}}{S}$	V/W

B. Numerical Simulations

We perform a suite of simulations with results (inverter output currents and terminal voltages) all shown in Fig. 8. Individual simulation setups, results, and inferences are discussed next.

1) Nominal Operation: The first simulation verifies steady-state phase balancing and power sharing among inverters with identical parameters. Pertinent waveforms are shown in Fig. 8(a); simulation results show phase-balanced operation and power sharing across the six inverters.

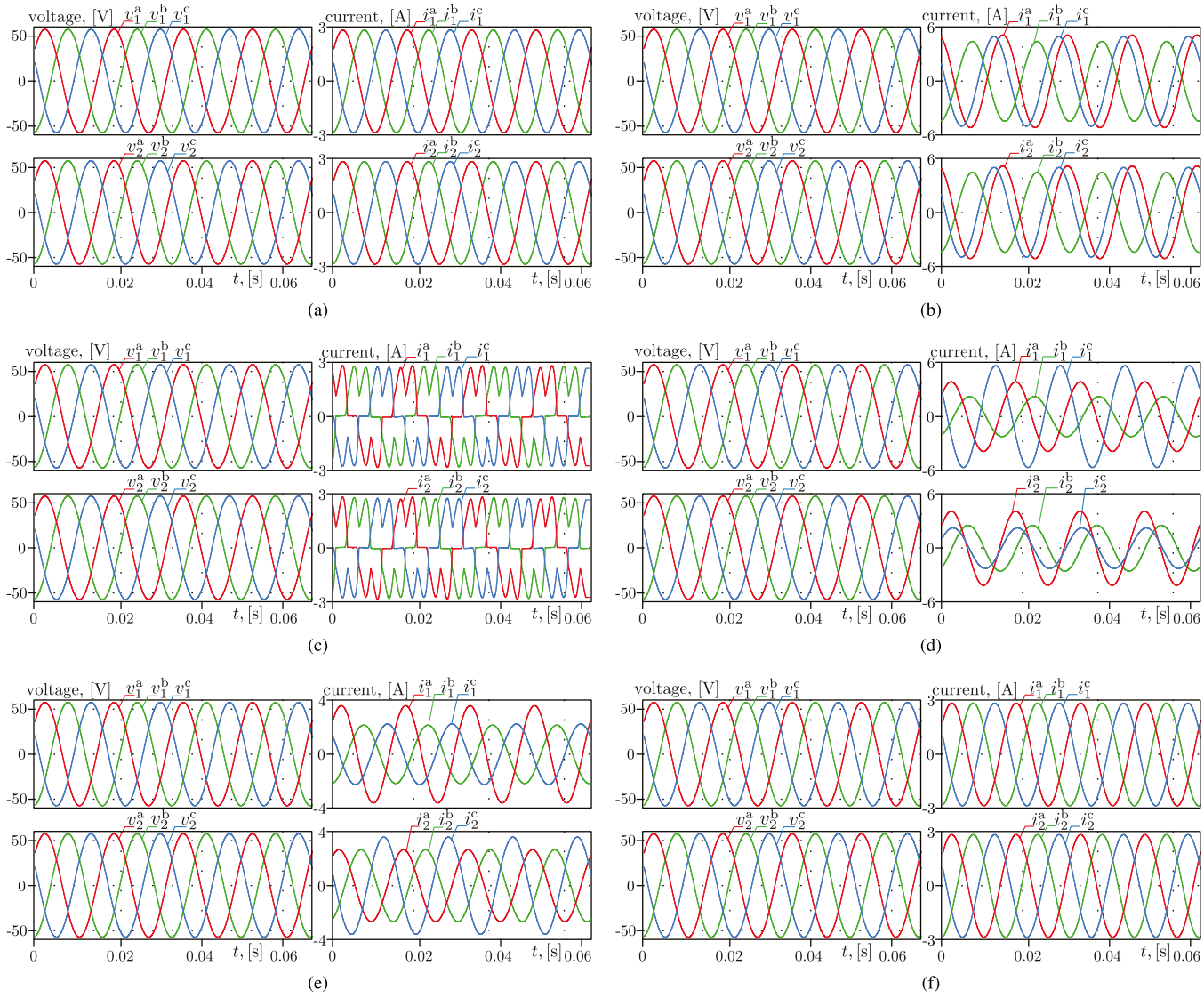

Fig. 8. Simulation results to demonstrate robustness of phase-balanced operation when symmetry and homogeneity assumptions leveraged in the analysis are challenged. (a) Nominal Operation. (b) Load Imbalance. (c) Nonlinear Loads. (d) Different power setpoints. (e) Different droop slopes. (f) Different Output-impedance R/X Ratios.

2) Load Imbalance: This simulation is conducted to show system maintaining phase-balancing and power sharing with imbalances in the three-phase loads. In particular, the three-phase local loads on the primary side of the transformer are set as: $5\overline{Z}_{\text{load,a}} = \overline{Z}_{\text{load,b}} = 0.2\overline{Z}_{\text{load,c}}$. The loads on the high-voltage side are maintained to be balanced. Results shown in Fig. 8(b) establish phase-balanced operation with power sharing between both sets of inverters.

3) Nonlinear Loads: This simulation verifies phase balancing and power sharing with nonlinear loads. In particular, deviating away from the linear loads assumed in the analysis and utilized in the remainder of the validation effort, we assume (nonlinear and appropriately rated) three-phase diode rectifier loads are connected at the low-voltage side of the transformer. As shown in Fig. 8(c), the terminal voltages of the inverters continue to be sinusoidal and phase balanced; the output currents are—as anticipated—non sinusoidal due to the rectifier loads.

4) Different Power Setpoints: The analytical developments were built on the supposition that the power setpoints are equal in a per-unit sense (by construction) and that they sum up to account for the load in the system (via some supervisory control effort). In real applications, these assumptions may not hold. In this simulation, we consider the setting where $P_1^\star = 100\,\text{W}$, $Q_1^\star = 200\,\text{VA}$, $P_2^\star = 100\,\text{W}$, $Q_2^\star = 100\,\text{VA}$, $P_3^\star = 150\,\text{W}$, $Q_3^\star = 50\,\text{VA}$, $P_4^\star = 150\,\text{W}$, $Q_4^\star = 50\,\text{VA}$, $P_5^\star = 200\,\text{W}$, $Q_5^\star = 100\,\text{VA}$, and $P_6^\star = 0\,\text{W}$, $Q_6^\star = 200\,\text{VA}$. Waveforms in Fig. 8(d) show that even with all six inverters having power setpoints that deviate away from the assumptions described above, phase-balanced operation can still be achieved.

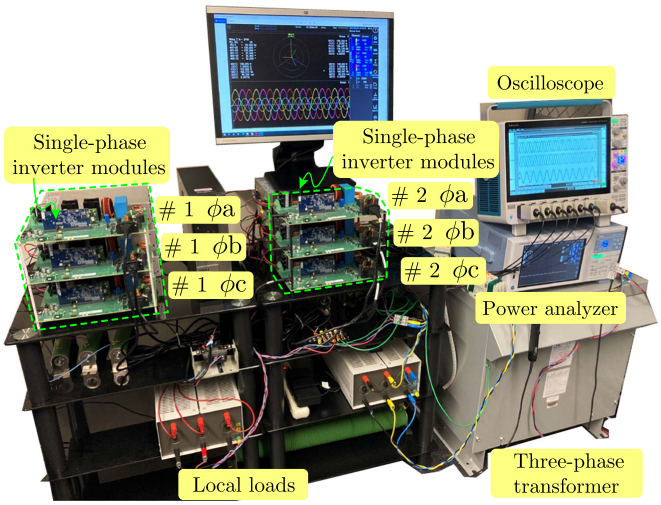

Fig. 9. Experimental system with six single-phase droop-controlled inverters, a transformer, and loads.

5) Different Droop Slopes: In this simulation, the single-phase inverters are programmed with droop slopes deviating away from the design specification in (5). For the frequency droop, the permissible frequency deviations are selected between 0.3 rad/s and 0.5 rad/s, randomly; specifically, $\Delta\omega_1 = 0.5 \times 2\pi$ rad/s, $\Delta\omega_2 = 0.4 \times 2\pi$ rad/s, $\Delta\omega_3 = 0.3 \times 2\pi$ rad/s, $\Delta\omega_4 = 0.4 \times 2\pi$ rad/s, $\Delta\omega_5 = 0.5 \times 2\pi$ rad/s, and $\Delta\omega_6 = 0.3 \times 2\pi$ rad/s. For the voltage droop, the permissible voltage deviations are also selected randomly, this time between 4% and 6%; specifically, $\Delta V_1 = 5\%$, $\Delta V_2 = 4\%$, $\Delta V_3 = 6\%$, $\Delta V_4 = 5\%$, $\Delta V_5 = 4\%$, and $\Delta V_6 = 5\%$. Waveforms in Fig. 8(e) show that phase balancing can still be achieved.

6) Different Output-Impedance R/X Ratios: In this simulation, we depart from the homogeneity assumption on output-impedance R/X ratios in (3). Particularly, we choose resistance $R \in [0.1,\ 0.3]\,\Omega$ and inductance $L \in [1,\ 3]$ mH. The R/X ratios range from 0.088 to 0.796. Simulation results in Fig. 8(f) indicate that this does not impact phase-balanced operation.

C. Experimental Results

The laboratory-scale prototype is shown in Fig. 9. A Texas Instruments TMS320F28379D microprocessor implements droop control with 5% and 0.5 Hz voltage and frequency droop, respectively. In addition to oscilloscope measurements, voltage, and current waveforms are also measured with a Yokogawa WT5000 power analyzer.

The full suite of experiments performed include the following.

1) Validation of phase-balanced behavior across phases and synchronized operation in each phase in steady state.
2) Maintenance of phase-balanced operation across phases during (large-signal) load step-up and load step-down transients.
3) System dynamics that clearly show convergence from an initially imbalanced condition towards phase-balanced operation once transformer-Δ coupling is introduced between phases.

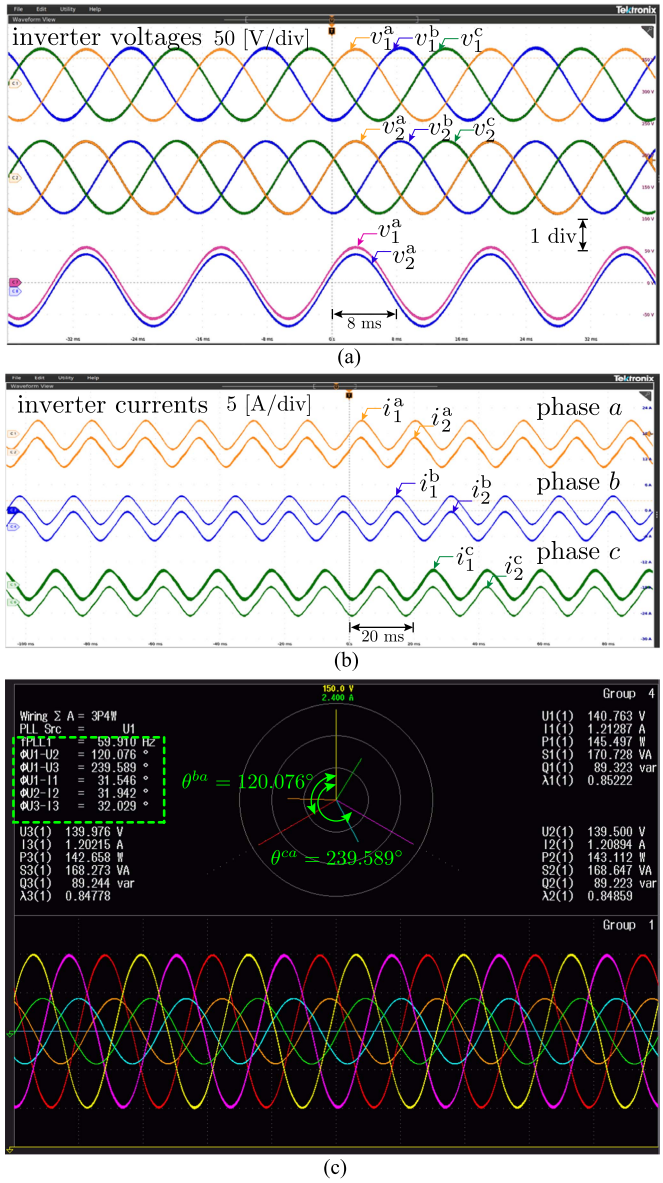

Fig. 10. Steady-state performance: (a) Voltages of six single-phase GFM inverters. (b) Current sharing within each phase. and (c) Voltages and currents at the transformer secondary terminals.

Overall, these experiments illustrate the robustness of the proposed approach in the face of large-signal disturbances and the validity of the analytical developments in establishing the feasibility of phase-balanced operation.

The first set of experimental results in Fig. 10 show the system in steady state during normal operation. Waveforms in Fig. 10(a) illustrate phase-balanced operation as well as synchronized voltages on each individual phase. The currents in Fig. 10(b) confirm that the inverters share power automatically. Line-to-line voltages and currents on the delta-connected side of the transformer are shown in Fig. 10(c). Power analyzer computations confirm that the relative angles are $\theta^{\text{ba}} \approx 120°$ and $\theta^{\text{ca}} \approx 240°$.

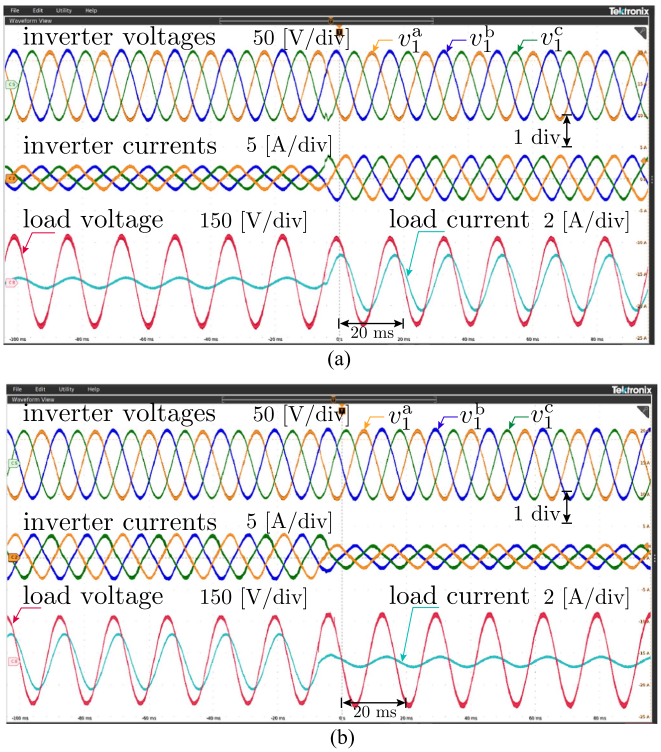

Fig. 11. Dynamic performance during load-step changes: (a) Loads step up, and (b) Loads step down. The system retains phase-balanced operation through these changes.

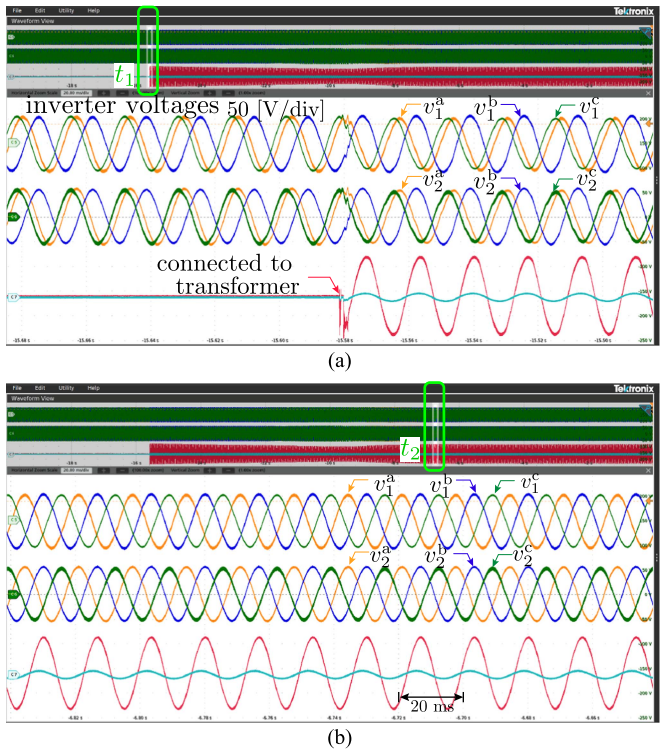

Fig. 12. Dynamic performance during startup: (a) Prior to the relay closing, the phase voltages are not balanced. (b) With the closure of the relay, the system achieves phase-balanced operation.

Next, we evaluate dynamic performance during transients with loads on the transformer secondary side undergoing step changes. Fig. 11(a) shows inverter voltages and currents as well as the voltage and current on the transformer secondary when P_{load} increases from 300 to 600 W. Performance during a load step down from 600 to 300 W is shown in Fig. 11(b). Evidently, the voltages across phases a, b, and c are able to maintain phase balancing during these transients.

Finally, we consider a start-up procedure with a relay interfacing the transformer to the inverter system. A series-connected resistor is used to limit inrush currents when the inverters are initially connected to the transformer. Measurements are shown in Fig. 12. Just before the relay is closed at t_1, it can be seen that inverters on each phase are synchronized to each other while waveforms between phases are imbalanced. After the relay is closed, the system converges to a phase-balanced steady state. Once the system is balanced at t_2, the start-up resistance is shorted out and the system maintains nominal operation from there forward.

The currents in Figs. 10 and 11 appear nonsinusoidal. Such phenomenon is attributed to the nonlinear magnetic properties of the three-phase transformer. This is typical in a distribution power transformer as was used in our experiment. In particular, the magnetizing inductance of a typical transformer has a nonlinear B-H curve, which gives rise to low order harmonics, especially third-order harmonics, within the current waveforms. In all cases, the voltages generated by the GFM inverters are sinusoidal.

VI. Conclusion and Future Work

In this article, we propose a method of using large numbers of single-phase GFM inverters to provide uninterrupted three-phase power. We prove that scores of droop-controlled inverters are able to simultaneously achieve power sharing while also giving phase balancing across distinct phases. This multitude of objectives is achieved without explicit communication channels and arises purely out of the inherent system dynamics. Taken together, this article establishes a vision for ultraresilient distribution systems as well as an accompanying analytical framework and experimental validation. As part of future work, it is pertinent to pursue analytical formulations and theoretical results that accommodate imbalances, nonuniformities, and are generally more reflective of practical setups. Additional threads of future research include investigating the behavior of other GFM primary-control methods, factoring in the source-side dynamics into pertinent models (and analysis), and evaluating performance in more complex networks.

Appendix

A. Establishing Power Sharing (11)

Let us begin with the active power sharing claim in (11a). The combination of (4b) and (5b) give the common steady-state

frequency for each phase as

$$\omega^{\phi} = \omega_{\text{nom}} - \Delta\omega_{\max}\left(\frac{P_k^{\phi}}{S_k^{\phi}} - \frac{P_k^{\phi\star}}{S_k^{\phi}}\right). \tag{38}$$

Rearranging terms, we can isolate

$$\frac{P_k^{\phi}}{S_k^{\phi}} = \frac{P_k^{\phi\star}}{S_k^{\phi}} + \frac{\omega_{\text{nom}} - \omega^{\phi}}{\Delta\omega_{\max}}. \tag{39}$$

Note that the right-hand side of (39) is a constant since it only depends on network-wide quantities/constants ($\omega_{\text{nom}}, \omega^{\phi}, \Delta\omega_{\max}$) and from (7) we recognize that the ratio $\frac{P_k^{\phi\star}}{S_k^{\phi}}$ is identical across all inverters in each phase. This establishes (11a).

Next, we consider the reactive power sharing claim in (11b). With the aid of (10a) and the voltage-droop law in (4a), we can obtain

$$\frac{Q_k^{\phi}}{S_k^{\phi}} = \frac{V^{\phi}(V_{\text{nom}} - V^{\phi}) + V^{\phi}\Delta V_{\max}\frac{Q_k^{\phi\star}}{S_k^{\phi}} - V_{\text{nom}}^2 R_{\text{pu}}\frac{P_k^{\phi}}{S_k^{\phi}}}{V_{\text{nom}}^2 X_{\text{pu}} + V^{\phi}\Delta V_{\max}}. \tag{40}$$

Note that the right-hand side of (40) depends only on network-wide quantities and constants (V^{ϕ}, V_{nom}, $\Delta V_{\max}$, R_{pu}, X_{pu}) as well as on the ratios $\frac{Q_k^{\phi\star}}{S_k^{\phi}}$ and $\frac{P_k^{\phi}}{S_k^{\phi}}$, which are identical for all inverters in each phase (as we can recognize from (7) and the prior discussion on active-power sharing). Therefore, we can conclude that the right-hand side of (40) is a constant, which establishes (11b).

B. Derivation of (17)

Consider the equivalent circuit shown in Fig. 5(b). Notice that the clockwise mesh currents in each phase branch are denoted by $\{\overline{I}_{\text{a1}}, \overline{I}_{\text{a2}}, \overline{I}_{\text{a3}}\}$, $\{\overline{I}_{\text{b1}}, \overline{I}_{\text{b2}}, \overline{I}_{\text{b3}}\}$, and $\{\overline{I}_{\text{c1}}, \overline{I}_{\text{c2}}, \overline{I}_{\text{c3}}\}$. For each phase, ϕ, we have the following set of equations that arise from application of Kirchhoff's laws and mesh analysis:

$$N^2\overline{Z}_{\text{load}}\overline{I}_{\phi 1} + N^2\overline{Z}_{\text{agg}}(\overline{I}_{\phi 1} - \overline{I}_{\phi 2}) + N\overline{V}_{\text{agg}}^{\phi} = 0 \tag{41a}$$

$$\overline{Z}_{\text{p}}\overline{I}_{\phi 2} + \overline{Z}_0(\overline{I}_{\phi 2} - \overline{I}_{\phi 3}) + N^2\overline{Z}_{\text{agg}}(\overline{I}_{\phi 2} - \overline{I}_{\phi 1}) - N\overline{V}_{\text{agg}}^{\phi} = 0 \tag{41b}$$

$$\overline{Z}_0(\overline{I}_{\phi 3} - \overline{I}_{\phi 2}) + \overline{Z}_{\text{s}}\overline{I}_{\phi 3} + \overline{Z}_{\text{load,s}}\sum_{k\in\Phi\setminus\phi}(\overline{I}_{\phi 3} - \overline{I}_{k3}) = 0. \tag{41c}$$

The values of the nine current phasors, $\{\overline{I}_{\phi 1}, \overline{I}_{\phi 2}, \overline{I}_{\phi 3}\}, \phi \in \Phi$ are obtained from the solution of the three sets of algebraic equations. Solving the expressions by hand is possible but an arduous process. To bypass this issue, we applied *Mathematica's* symbolic solver to compute the mesh currents in closed form. The current flowing through the aggregated inverter model $\overline{I}_{\phi}$, which is the difference of $\overline{I}_{\phi} = \overline{I}_{\phi 2} - \overline{I}_{\phi 1}$, can be expressed as

$$\overline{I}_{\phi} = \frac{N}{\overline{Z}_{\text{eq1}}}\sum_{k\in\Phi}\overline{V}_{\text{agg}}^{k} + \frac{N}{\overline{Z}_{\text{eq2}}}\overline{V}_{\text{agg}}^{\phi} \tag{42}$$

where $\overline{Z}_{\text{eq1}}$ and $\overline{Z}_{\text{eq2}}$ are equivalent impedances containing system impedance information, including the transformer impedances and inverter output impedances. The closed-form expressions of $\overline{Z}_{\text{eq1}}$ and $\overline{Z}_{\text{eq2}}$ are

$$\overline{Z}_{\text{eq1}} = \frac{\alpha_1\alpha_2}{\overline{Z}_0^2\overline{Z}_{\text{load}}^2\overline{Z}_{\text{load,s}}}, \quad \overline{Z}_{\text{eq2}} = \frac{N^2\alpha_2}{\alpha_3} \tag{43}$$

where

$$\begin{aligned}
\alpha_1 &= N^2\overline{Z}_{\text{agg}}\overline{Z}_{\text{load}}(\overline{Z}_0 + \overline{Z}_{\text{s}}) \\
&\quad + (\overline{Z}_{\text{agg}} + \overline{Z}_{\text{load}})(\overline{Z}_{\text{p}}\overline{Z}_{\text{s}} + \overline{Z}_0(\overline{Z}_{\text{p}} + \overline{Z}_{\text{s}})) \\
\alpha_2 &= (N^2\overline{Z}_{\text{agg}}\overline{Z}_{\text{load}} + (\overline{Z}_{\text{agg}} + \overline{Z}_{\text{load}})\overline{Z}_{\text{p}})(3\overline{Z}_{\text{load,s}} + \overline{Z}_{\text{s}}) \\
&\quad + \overline{Z}_0(\overline{Z}_{\text{load}}(3\overline{Z}_{\text{load,s}} + \overline{Z}_{\text{p}} + \overline{Z}_{\text{s}}) \\
&\quad + \overline{Z}_{\text{agg}}(3\overline{Z}_{\text{load,s}} + N^2\overline{Z}_{\text{load}} + \overline{Z}_{\text{p}} + \overline{Z}_{\text{s}})) \\
\alpha_3 &= (N^2\overline{Z}_{\text{load}} + \overline{Z}_{\text{p}})(3\overline{Z}_{\text{load,s}} + \overline{Z}_{\text{s}}) \\
&\quad + \overline{Z}_0(3\overline{Z}_{\text{load,s}} + N^2\overline{Z}_{\text{load}} + \overline{Z}_{\text{p}} + \overline{Z}_{\text{s}}).
\end{aligned}$$

The apparent power delivered by each aggregated inverter in phase $\phi \in \Phi$ is given by

$$\overline{S}^{\phi} = N\,\overline{V}_{\text{agg}}^{\phi}\,\overline{I}_{\phi}^{*}. \tag{44}$$

The real and imaginary parts of (44) yield the active- and reactive-power expressions given in (17).

REFERENCES

[1] National Renewable Energy Laboratory, "Grid-forming inverter controls," Accessed: Jan. 10, 2023. [Online]. Available: https://www.nrel.gov/grid/grid-forming-inverter-controls.html

[2] X. Wang, "Resurgence of grid-forming inverter technology," *IEEE Electrific. Mag.*, vol. 10, no. 1, pp. 5–6, Mar. 2022.

[3] M. Lu, S. Dhople, D. Zimmanck, and B. Johnson, "Spontaneous phase balancing in delta-connected single-phase droop-controlled inverters," *IEEE Trans. Power Electron.*, vol. 37, no. 12, pp. 14115–14125, Dec. 2022.

[4] M. Pilehvar, D. Sharma, and B. Mirafzal, "Forming interphase microgrids in distribution systems using cooperative inverters," *CPSS Trans. Power Electron. Appl.*, vol. 7, no. 2, pp. 186–195, 2022.

[5] A. Hintz, U. Prasanna, and K. Rajashekara, "Comparative study of the three-phase grid-connected inverter sharing unbalanced three-phase and/or single-phase systems," *IEEE Trans. Ind Appl.*, vol. 52, no. 6, pp. 5156–5164, Nov./Dec. 2016.

[6] Y. Karimi, H. Oraee, and J. M. Guerrero, "Decentralized method for load sharing and power management in a hybrid single/three-phase-islanded microgrid consisting of hybrid source PV/Battery units," *IEEE Trans. Power Electron.*, vol. 32, no. 8, pp. 6135–6144, Aug. 2017.

[7] S. Nudehi and D. Groß, "Grid-forming control of three-phase and single-phase converters across unbalanced transmission and distribution systems," *IEEE Trans. Power Syst.*, vol. 38, no. 6, pp. 5687–5700, Nov. 2023.

[8] R. W. Kenyon et al., "Stability and control of power systems with high penetrations of inverter-based resources: An accessible review of current knowledge and open questions," *Sol. Energy*, vol. 210, pp. 149–168, 2020.

[9] M. Sinha, J. Poon, B. B. Johnson, M. Rodriguez, and S. V. Dhople, "Decentralized interleaving of parallel-connected buck converters," *IEEE Trans. Power Electron.*, vol. 34, no. 5, pp. 4993–5006, May 2019.

[10] M. Sinha, F. Dörfler, B. Johnson, and S. Dhople, "Stabilizing phase-balanced or phase-synchronized trajectories of Van der Pol oscillators in uniform electrical networks," in *Proc. 56th Annu. Allerton Conf. Commun., Control, Comput.*, 2018, pp. 335–340.

[11] M. Sinha, F. Dörfler, B. Johnson, and S. Dhople, "Phase balancing in globally connected networks of liénard oscillators," in *Proc. IEEE 56th Annu. Conf. Decis. Control*, 2017, pp. 595–600.

[12] D. Paley, N. Leonard, and R. Sepulchre, "Oscillator models and collective motion: Splay state stabilization of self-propelled particles," in *Proc. 44th IEEE Conf. Decis. Control*, 2005, pp. 3935–3940.
[13] R. Sepulchre, D. A. Paley, and N. E. Leonard, "Stabilization of planar collective motion: All-to-all communication," *IEEE Trans. Autom. Control*, vol. 52, no. 5, pp. 811–824, May 2007.
[14] V. Purba, B. B. Johnson, S. Jafarpour, F. Bullo, and S. V. Dhople, "Dynamic aggregation of grid-tied three-phase inverters," *IEEE Trans. Power Syst.*, vol. 35, no. 2, pp. 1520–1530, Mar. 2020.
[15] P. J. Hart, R. H. Lasseter, and T. M. Jahns, "Coherency identification and aggregation in grid-forming droop-controlled inverter networks," *IEEE Trans. Ind. Appl.*, vol. 55, no. 3, pp. 2219–2231, May/Jun. 2019.
[16] N. Shabanikia and S. A. Khajehoddin, "Weighted dynamic aggregation modeling of grid-following inverters to analyze renewable DG integrated microgrids," *IEEE Trans. Indust. Electron.*, vol. 71, no. 1, pp. 583–594, Jan. 2024.
[17] A. M. S. Al-bayati, F. Mancilla-David, and J. L. Domínguez-Garcíal, "Aggregated models of wind farms: Current methods and future trends," in *Proc. North Amer. Power Symp.*, 2016, pp. 1–6.
[18] B. Johnson, M. Rodriguez, M. Sinha, and S. Dhople, "Comparison of virtual oscillator and droop control," in *Proc. 18th Workshop Control Model. Power Electron.*, 2017, pp. 1–6.
[19] M. Lu, V. Purba, S. Dhople, and B. Johnson, "Comparison of droop control and virtual oscillator control realized by Andronov-Hopf dynamics," in *Proc. 46th Annu. Conf. IEEE Indust. Electron. Soc.*, 2020, pp. 4051–4056.
[20] F. Dörfler and F. Bullo, "Synchronization in complex networks of phase oscillators: A survey," *Automatica*, vol. 50, no. 6, pp. 1539–1564, 2014.
[21] J. W. Simpson-Porco, F. Dörfler, and F. Bullo, "Droop-controlled inverters are Kuramoto oscillators," *IFAC Proc. Volumes*, vol. 45, no. 26, pp. 264–269, 2012.
[22] H. Min, F. Paganini, and E. Mallada, "Accurate reduced-order models for heterogeneous coherent generators," *IEEE Contr. Syst. Lett.*, vol. 5, no. 5, pp. 1741–1746, Nov. 2021.
[23] O. Ajala, N. Baeckeland, B. Johnson, S. Dhople, and A. Domínguez-García, "Model reduction and dynamic aggregation of grid-forming inverter networks," *IEEE Trans. Power Syst.*, vol. 38, no. 6, pp. 5475–5490, Nov. 2023.
[24] O. Ajala, N. Baeckeland, S. Dhople, and A. Domínguez-García, "Uncovering the Kuramoto model from full-order models of grid-forming inverter-based power networks," in *Proc. 60th IEEE Conf. Decis. Control*, 2021, pp. 4944–4949.
[25] H. K. Khalil, *Nonlinear Systems*. 3rd ed., vol. 115. Frisco, TX, USA: Patience Hall, 2002.

Minghui Lu (Member, IEEE) received the B.E. degree in electrical engineering from the Harbin Institute of Technology, Harbin, China, in 2011, the M.S. degree in electrical engineering from the Huazhong University of Science and Technology, Wuhan, China, in 2014, and the Ph.D. degree in power electronics from Aalborg University, Aalborg, Denmark in 2017.

He is currently a Research Engineer with Pacific Northwest National Laboratory (PNNL). Prior to joining PNNL, he was a Research Associate with the University of Washington Seattle and University of Texas at Austin, respectively. His research interests include power electronics, grid-forming inverters, and modeling and control of power electronics. He was the recipient of the 2022 IEEE TRANSACTIONS ON POWER ELECTRONICS (Second Place) Prize Paper Award and was recognized with the 2020 IEEE TRANSACTIONS ON ENERGY CONVERSION Outstanding Reviewer Award.

Weiqian Cai (Student Member, IEEE) received the B.E. and M.S. degrees in electrical engineering from Tsinghua University, Beijing, China, in 2017 and 2020, respectively. He is currently working toward the Ph.D. degree with the Chandra Family Department of Electrical and Computer Engineering, The University of Texas at Austin, Austin, TX, USA.

Prior to that, he was a Ph.D. student with the University of Washington, Seattle, WA, USA. His research focuses on modeling and control of inverters with a focus on grid-forming applications.

Sairaj Dhople (Senior Member, IEEE) received the B.S., M.S., and Ph.D. degrees in electrical engineering from the University of Illinois at Urbana-Champaign, Urbana, IL, USA, in 2007, 2009, and 2012, respectively.

He is currently Robert and Sydney Anderson Professor with the Department of Electrical and Computer Engineering, University of Minnesota, Minneapolis, MN, USA. His research interests include modeling, analysis, and control of power electronics and power systems with a focus on renewable integration.

Dr. Dhople was the recipient of the National Science Foundation CAREER Award in 2015, Outstanding Young Engineer Award from the IEEE POWER AND ENERGY SOCIETY in 2019, 2021 IEEE Power and Energy Society Prize Paper Award, and the 2022 IEEE TRANSACTIONS ON POWER ELECTRONICS (Second Place) Prize Paper Award.

Brian Johnson (Senior Member, IEEE) received the M.S. and Ph.D. degrees in electrical and computer engineering from the University of Illinois at Urbana-Champaign, Urbana, IL, USA, in 2010 and 2013, respectively.

He is currently an Assistant Professor and a Fellow of the Jack Kilby/Texas Instruments Endowed Faculty Fellowship in Computer Engineering with the Chandra Family Department of Electrical and Computer Engineering, The University of Texas at Austin, Austin, TX, USA. Previously, he was the Washington Research Foundation Innovation Assistant Professor within the Department of Electrical and Computer Engineering, University of Washington in Seattle, Seattle, WA, USA. Prior to joining the University of Washington in 2018, he was an Engineer with the National Renewable Energy Laboratory. He is currently coleading the multi-institutional Universal Interoperability for Grid-Forming Inverters (UNIFI) Consortium which is funded by the U.S. Department of Energy. His research interests include renewable energy systems, power electronics, and control systems.

His work was recognized with a National Science Foundation CAREER Award in 2022 as well as prize paper awards from the IEEE TRANSACTIONS ON ENERGY CONVERSION and IEEE TRANSACTION ON POWER ELECTRONICS.